First principles investigation into the interwoven nature of voltage and mechanical

properties of the Li<sub>x</sub>NMC-811 cathode

Michael Woodcox, Robert Shepard, Manuel Smeu\*

Department of Physics, Binghamton University - SUNY, Binghamton, NY 13902, USA

Abstract

Density functional theory has been used to investigate the electrochemical and mechanical properties of the well-known

cathode material Li<sub>x</sub>Ni<sub>0.833</sub>Mn<sub>0.083</sub>Co<sub>0.083</sub>O<sub>2</sub> (Li<sub>x</sub>-NMC-811) as a function of Li concentration. We used the PBE

functional with dispersion corrections to calculate a voltage in good agreement with experiment, which gradually changes

from 3.3 to 4.2 V during the charging process. A similar profile trend can be found without dispersion, though voltages

were lower by  $\sim 0.4 \text{ V}$  and the known NMC lattice collapse was not captured as it was with dispersion. We compare

calculated quantities such as Young's modulus (E) to better understand the mechanical response of the material to

outside forces with varying Li concentration. We also compare Poisson's ratio  $(\nu)$  and the Pugh ratio  $(\gamma)$ , which are used

as metrics of ductility, for each of these lithiation concentrations. We have shown that as the concentration of Li reaches

x = 0.25, the material transitions from ductile to brittle based on both ductility metrics. It is near this concentration

that we also see the largest change in voltage from our calculations. We propose that this transition between ductile

and brittle provides additional insight and understanding to structural failure and, consequently, capacity loss during

normal cycling for cathode materials. Furthermore, it demonstrates a mechanism for reversibly controlling mechanical

properties by electrochemical means.

Keywords: Density functional theory, NMC, energy storage, mechanical properties, ductility

1. Introduction

Since its development in the latter half of the 20<sup>th</sup> cen-

tury, the Li ion battery (LIB) has revolutionized nearly

every aspect of our daily lives [1, 2]. Its high energy den-

sity and specific capacity has led to its use in many mod-

ordy wird specific corporate in many mode

ern electronic devices. However, there has been a recent

\*Corresponding author

Email address: msmeu@binghamton.edu (Manuel Smeu)

Preprint submitted to Journal of Power Sources

demand for improved performance, lower cost, better stability, and lower environmental impact [3, 4, 5, 6], which

has led to the use of materials design to optimize the per-

formance of current battery cathodes [7, 3, 8, 9, 10]. Al-

though various transition metal oxides have been inves-

tigated [11, 12, 13], the tunable nature of Ni<sub>a</sub>Mn<sub>b</sub>Co<sub>c</sub>O<sub>2</sub>

(where a + b + c = 1), has made it a front runner for

use in LIBs [9, 14].

Throughout various investigations,  $Ni_aMn_bCo_cO_2$ (NMC-abc) compounds have been shown to possess desirable characteristics such as high specific capacities and the ability to achieve high voltages. Although having shown the capability to reach well over 4 V, NMC cathodes are typically unable to compete with the industry standard of  $\sim 300$  mAh g<sup>-1</sup> for specific capacity in LIBs [9, 14, 15, 16, 17]. Despite their promising electrochemical performance and extensive use within industry, several reported issues have plagued NMC compounds. In particular, mechanical failure as a result of changes to the structure that regularly occurs during cycling [15, 18, 19, 20]. As the structure moves towards failure, cavitation and fracturing contribute to a degradation in the quality of the material [14, 18]. This less stable structure results in a decreased capacity for the cathode, as well as altering the overall integrity of the entire battery which weakens conduction, reduces efficiency, and is known to cause catastrophic failure of batteries [21, 22, 23, 24, 25, 14]. Previous works have investigated the effects of stress accumulation within battery interfaces [26, 27], where failures will occur at the brittle interfaces because of the inability to accommodate the stress introduced to the system during charge/discharge cycling [28]. Due to these failures, it has become a necessary part of battery research to thoroughly explore the mechanical properties of all components [29].

Despite increased difficulty in performing mechanically

driven experiments on NMC materials due to their reactive nature with air [30], there are various concentrations of NMC of which the mechanical properties have been investigated to some extent (e.g., NMC-333, NMC-442, NMC-532, NMC-622, and NMC-811) with a mixture of experimental and computational results [16, 17, 9, 14]. Throughout these works there is significant investigation of the Young's modulus and hardness of these various NMC materials [17, 9, 14], with additional investigations into Poisson's ratio [17], the coefficient of thermal expansion [9], and interfacial fracture toughness [14]. Additional thermal quantities (including Helmholtz free energy, vibrational entropy, and specific heat) have also been studied to some extent [9]. Most notably, this collection of previous work indicates that each of these structural properties (Young's modulus, hardness and overall mechanical strength) will decrease overall as the battery is continually cycled [16, 17, 9, 14]. There is a significant amount of data for NMC-abc compounds, however, there is a lack in consistency in reporting of particular properties of interest, which makes it very challenging to draw any conclusions on the overall mechanical properties of these battery materials. It would be of great benefit to focus research efforts into developing a database of such properties.

In this work, we use first-principles density functional theory (DFT) calculations to investigate the electrochemical and mechanical properties of  ${\rm Li}_x{\rm Ni}_{0.833}{\rm Mn}_{0.083}{\rm Co}_{0.083}{\rm O}_2$  (hereafter referred to as NMC-811) as a function of Li concentration. Calculation

of the bulk (K) and shear (G) moduli provide us with enough information to compute Young's (E) modulus, as well as Poisson's ratio  $(\nu)$  and the Pugh ratio  $(\gamma)$ , which we use to investigate changes in ductility through various intercalation concentrations. We are then able to compare these mechanical quantities to the calculated voltage profile of  $\text{Li}_x\text{NMC-811}$  to further investigate the implications of changes in such properties.

## 2. Computational methods

#### 2.1. Computational details

DFT calculations were performed using the Vienna Abinitio Simulation Package (VASP) [31, 32, 33, 34, 35, 36]. VASP uses a plane wave basis set, and ion-electron interactions were approximated using the projector augmented wave (PAW) potentials [37]. Both the kinetic energy cutoff and k-point grid were tested with the criterion for convergence being an energy variation of less than 1 meV/atom. A plane wave energy cutoff of 700 eV and a  $\Gamma$ -centered  $3\times3\times1$  Monkhorst-Pack [38] k-point grid were found to be sufficient for all calculations. The Brillouin zone was sampled by the use of Gaussian smearing and all structural relaxations and energy calculations were performed using the Perdew-Burke-Ernzerhof (PBE) functional [39], both with and without the inclusion of van der Waals (vdW) interactions by means of the zero-damping method (DFT-D3) of Grimme [40].

## 2.2. Relaxations

A full structural relaxation, including lattice vectors, was performed on the fully lithiated (i.e.,

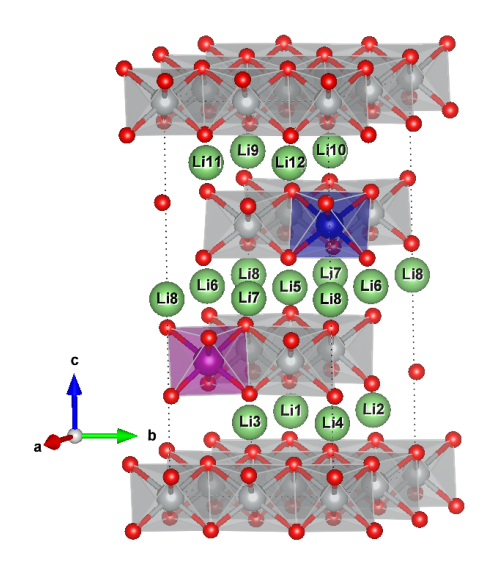


Figure 1: The Li-NMC-811 cell shown in color with Li (green), O, (red), Ni (gray), Co (blue) and Mn (purple), with each intercalation site labeled. Crystallographic information for this structure can be found in Table S1 in the Supplemental Material [41].

 $Li_1Ni_{0.833}Mn_{0.083}Co_{0.083}O_2$ , or Li-NMC-811), material. The initial atomic configuration (where the supercell, modeled after Ref. [42], is in the  $R\bar{\jmath}m$  space group) is provide in Table S1 [41]. Deintercalation of Li (i.e., charging) was simulated by a sequence of configuration comparisons (i.e., site testing). For example, the structure of one Li atom being removed from Fig. 1 (x = 0.917) was determined by comparing the energy of all possible configurations resulting from a single Li atom being removed from the 12 octahedral sites within our simulation cell. Then, the lowest energy configuration was kept as the final structure for this Li concentration. This structure was then used to determine the lowest energy configuration for x = 0.833 by comparing the energies of individually removing each of the remaining 11 Li atoms. This process was repeated until the cathode was completely void of Li, with each of the most energetically favorable structures being used in all ensuing calculations. This procedure

yielded the following as the most energetically favorable sequence for removing Li atoms: 4, 7, 12, 1, 6, 10, 8, 3, 11, 2, 9, 5 for PBE and 11, 5, 3, 8, 10, 4, 7, 12, 1, 2, 9, 6 for PBE-D3, with the numbers corresponding to the labels in Fig. 1. Because we are using a relatively small cell to simulate our system, we are limited in the possible number of Li concentrations which can be investigated. A more detailed landscape would provide more insight into the overall mechanical nature of the NMC-811 cathode; however, the current work provides the groundwork for further exploration into alternate Li concentrations.

Upon completion of the site testing, formation energies were computed for all Li concentrations. Formation energy,  $E_{\text{Form}}$ , was computed using

$$E_{\text{Form}} = E_{\text{Li}_x \text{NMC}} - x E_{\text{Li-NMC}} - (1-x) E_{\text{NMC}} . \tag{1}$$

In the above equation,  $E_{\text{Li}_x \text{NMC}}$  is the energy of the partially intercalated NMC-811 cathode,  $E_{\text{Li-NMC}}$  is the energy of the fully intercalated cathode (as shown in Fig. 1), and  $E_{\text{NMC}}$  is the energy of the fully delithiated NMC-811 structure. After  $E_{\text{Form}}$  was determined, a convex hull was created (see Fig. S1 [41]) to determine the stability of each Li concentration structure.

## 2.3. Voltage

To compute voltages for our simulated charging process, we focus on the half-reactions

$$\text{Li}_x \text{NMC} \to \text{Li}_y \text{NMC} + 12(x-y)\text{Li}^+ + 12(x-y)e^-$$

and

$$\mathrm{Li}^+ + e^- \to \mathrm{Li}_{\mathrm{metal}}$$

for the cathode and anode, respectively, where x and y are Li concentrations such that x > y. It should be noted that the "12" in the cathode half-reaction is due to the supercell used (*i.e.*, 12 total Li ions). The combination of these half-reactions yields the overall reaction of

$$\text{Li}_x \text{NMC} \to \text{Li}_y \text{NMC} + 12(x - y) \text{Li}_{\text{metal}}$$
.

This overall reaction corresponds to 12(x-y) electrons being transferred from the cathode to the anode when delithiating 12(x-y) Li atoms from NMC-811. It then follows that voltage can be calculated as

$$V = \frac{\left(E_{\text{Li}_y \text{NMC}} + 12(x - y)E_{\text{Li}_{\text{metal}}}\right) - E_{\text{Li}_x \text{NMC}}}{12(x - y)}, \quad (2)$$

where  $E_{\text{Li}_y \text{NMC}}$  and  $E_{\text{Li}_x \text{NMC}}$  are the energies of  $\text{Li}_y \text{NMC}$ -811 and  $\text{Li}_x \text{NMC-811}$ , respectively, and  $E_{\text{Li}_{\text{metal}}}$  is the energy per atom of a pure Li metal anode. This process was utilized only for those intercalation concentrations residing on the convex hull in Fig. S1 [41] to create the final voltage profile shown in Fig. 3.

The calculation of voltage in this manner is an approximation since volume and entropy effects are neglected and only the internal energy of each system is considered. Inclusion of volume and entropy effects has been shown to contribute less than 0.2 V while greatly increasing computational cost [43, 44, 45, 46, 47, 48]. In addition, all surface interactions have been neglected in this work as it is assumed that ions can readily intercalate within the bulk of NMC-811 based on previous experimental works [49, 50, 51, 52, 53, 54, 55, 56, 57, 58].

# 2.4. Elastic properties

In previous work [59, 60, 29], we have shown that the elements of the elastic tensor  $(C_{ij})$  can be calculated using the generalized stress-strain variant of Hooke's Law,

$$\sigma_i = C_{ij}\epsilon_j \ , \tag{3}$$

where  $\sigma_i$  and  $\epsilon_j$  are the stress and strain, respectively. This requires that after completing the structural relaxation, we apply an artificial strain along one dimension ( $\pm$  0.5% and  $\pm$  1.0%) and two dimensions ( $\pm$  3.0% and  $\pm$  6.0%). The internal stress of the system is calculated along each possible axis of applied strain in individual simulations. This tensor provides us with sufficient information to calculate the bulk modulus (K) and the shear modulus (G) for a given material (calculated values are provided in Table S4 of the Supplemental Material [41]). We use the Voigt-Reuss-Hill (VRH) approximation to extract polycrystalline properties from single crystal data [61]. We use the following equations to obtain the upper bound of K and G,

$$K_{\rm V} = \frac{1}{9}(C_{11} + C_{22} + C_{33}) + \frac{2}{9}(C_{12} + C_{23} + C_{13}),$$
 (4)

$$G_{V} = \frac{1}{15}(C_{11} + C_{22} + C_{33}) - \frac{1}{15}(C_{12} + C_{23} + C_{13}) + \frac{1}{5}(C_{44} + C_{55} + C_{66}).$$
 (5)

To obtain the Reuss variants of K and G (i.e., the lower bound), we use the inverse of the elastic tensor (the compliance tensor), where  $S_{ij}$  are the matrix elements of the compliance tensor, allowing us to calculate  $K_R$  and  $G_R$ ,

$$\frac{1}{K_{\rm R}} = (S_{11} + S_{22} + S_{33}) + 2(S_{12} + S_{23} + S_{13}) , \qquad (6)$$

$$\frac{1}{G_{\rm R}} = \frac{4}{15} (S_{11} + S_{22} + S_{33}) - \frac{4}{15} (S_{12} + S_{23} + S_{13}) + \frac{1}{5} (S_{44} + S_{55} + S_{66}) .$$
(7)

The (VRH) averages for K and G can be calculated as

$$K = \sqrt{K_{\rm V} K_{\rm R}} , \qquad (8)$$

$$G = \sqrt{G_{\rm V}G_{\rm R}} \ . \tag{9}$$

With the calculated quantities K and G, we are able to compute additional physical properties such as Young's modulus (E), Poisson's ratio  $(\nu)$ , and the Pugh ratio  $(\gamma)$ ,

$$E = \frac{9KG}{3K + G} \,, \tag{10}$$

$$\nu = \frac{3K - 2G}{2(3K + G)} \,\,, \tag{11}$$

$$\gamma = \frac{K}{G} \ . \tag{12}$$

We have used both Poisson's ratio and the Pugh ratio in previous work as calculated metrics of ductility [59, 60, 29]. Since these particular quantities are determined from K and G, they offer a straightforward method of predicting ductility from first principles. As a general guide, a material with a Pugh ratio greater than 1.75 is ductile, whereas one with a Pugh ratio less than 1.75 is brittle [62]. This is a common technique used for assigning ductility to a material even though Pugh's original works were related to phenomenological findings [62]. Similarly, Poisson's ratio is another dimensionless quantity that is used as a metric for ductility. A Poisson's ratio greater than 0.26 indicates ductility, while a Poisson's ratio less than 0.26 denotes brittleness. This technique is typically applied to other materials (alloys, etc.), but we expect it to be insightful

for cathode analysis. The question of its reliability is of great interest, though we expect dramatic changes in the Poisson's and Pugh ratios to reflect changes in ductility, even if the exact boundary value is different from that typically used in other materials.

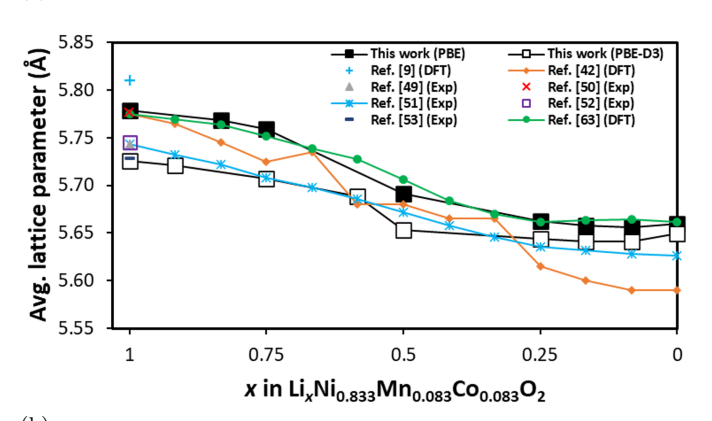
## 3. Results and discussion

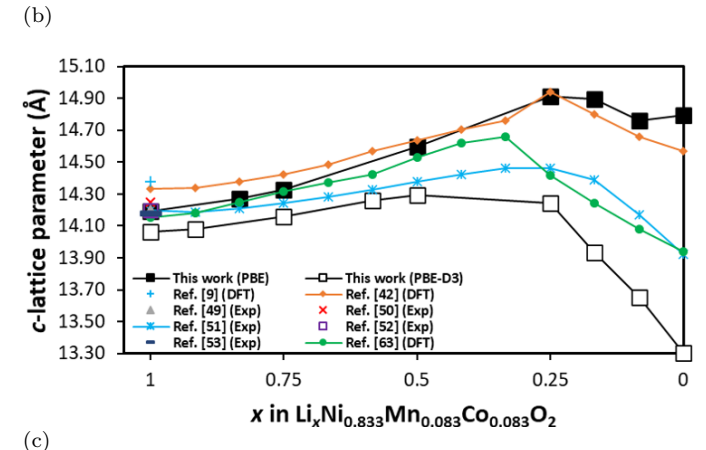
# 3.1. Structure and Site Testing

With and without the inclusion of dispersion effects, the resulting structural relaxations maintained the  $R\bar{\beta}m$  crystal structure for the fully lithiated and delithiated structures as shown in Fig. 1. The resulting averaged a, b-lattice vector, c-lattice vector, and cell volume are shown in Fig. 2, as a function of Li concentration with comparison between various other computational [42, 63, 64] and experimental works [49, 50, 51, 52, 53] (numerical values of all lattice parameters are shown in Tables S2 and S3 for PBE and PBE-D3, respectively [41]). Throughout delithiation, the a, b-lattice vector undergoes a general trend of contracting. From fully lithiated to fully delithiated, the vector only undergoes a 2.0% and 1.3% decrease for PBE and PBE-D3, respectively. As shown in Fig. 2a, both PBE and PBE-D3 are in good agreement with other works, while PBE-D3 has better overall agreement with experimental works [49, 50, 51, 52, 53].

With the c-lattice vector (Fig. 2b), we find a general expansion from fully lithiated to x = 0.25 in  $\text{Li}_x\text{NMC-811}$  for PBE. After this concentration, PBE undergoes a slight contraction at x = 0.083. With PBE-D3, the structure

(a)





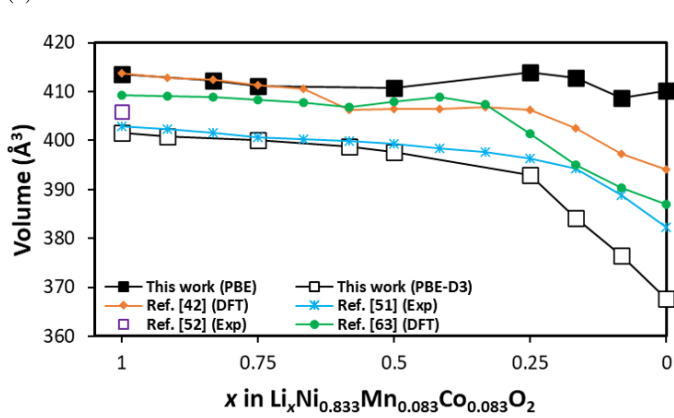


Figure 2: Resulting (a) a, b-lattice vector average, (b) c-lattice vector, and (c) cell volume during the delithiation process for this work and others [9, 42, 63, 49, 50, 51, 52, 53].

initially expands until x = 0.5. Following this, the material undergoes a lattice collapse from x = 0.25 to full delithiation, in agreement with previous works [51, 63]. With the behavior of lattice vectors a, b and c, the volume (Fig. 2c) for PBE remains fairly unchanged (changing

by only 0.81%) during the delithiation process. However, when we include dispersion, the collapse of the c-lattice vector causes a larger decrease in volume (8.44%).

The results of the relative formation energy calculations using PBE and PBE-D3 are shown in Fig. S1, with the numerical results of the calculations also provided in Tables S2 and S3 [41]. For all mechanical properties calculations, each concentration was investigated but only values which lie on the hull are shown in this work, while all other values are provided in Table S4 [41].

# 3.2. Voltage

Using the results shown in Fig. S1 [41] and Eqn. 2, voltages were calculated for each stable  $\text{Li}_x\text{NMC-811}$  system and are presented in Fig. 3. Voltages are only calculated for concentrations which lie on the convex hull as they are the only ones expected to be thermodynamically stable. We note that lithium is unlikely to be entirely extracted in the experiment, but we are interested in determining how the properties change throughout the delithiation process, leading to calculations of the mechanical properties at multiple concentrations from x = 1 to x = 0. While some of the values we calculate may not be achieved experimentally, they offer valuable insights into how the cathode properties change in extreme conditions. When dispersion effects are included, the largest change in our calculated voltages occur when charging from x = 0.25 to x = 0.167. Without dispersion, the largest change occurs from x = 0.167 to x = 0.083. Further discussion on these changes can be found in Sec. 4.

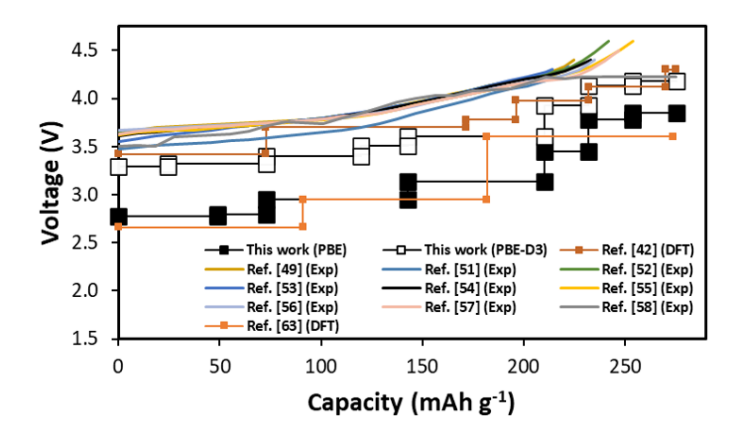


Figure 3: Calculated voltage for each stable  $\operatorname{Li}_x \operatorname{NMC-811}$  system using PBE and PBE-D3 (filled and empty black squares, respectively). Other DFT (small squares) and experimental (curved lines) works are included as well.

Results from experimental [49, 51, 52, 53, 54, 55, 56, 57, 58] and computational [42, 63] investigations are also reported on Fig. 3 for comparison. It can be seen that standard DFT (PBE) underestimates the voltage when compared to experiment, whereas the inclusion of dispersion effects (PBE-D3) yields voltages in better agreement with previously reported values. Due to the agreement between our calculated values and reported experimental values for the structural and electrochemical properties, we believe that a sufficient level of theory has been reached with PBE-D3.

## 3.3. Mechanical Properties

#### 3.3.1. Elastic Moduli

The resulting calculations for the bulk (K), shear (G) and Young's (E) moduli are shown in Fig. 4a, with numerical values for all calculated properties with PBE and PBE-D3 provided in Table S4 [41]. For concentrations of  $x \geq 0.5$ , each of the elastic moduli are almost unchanged (for changes in concentration, and across functionals). For  $x \leq 0.25$  the values diverge when comparing the calcula-

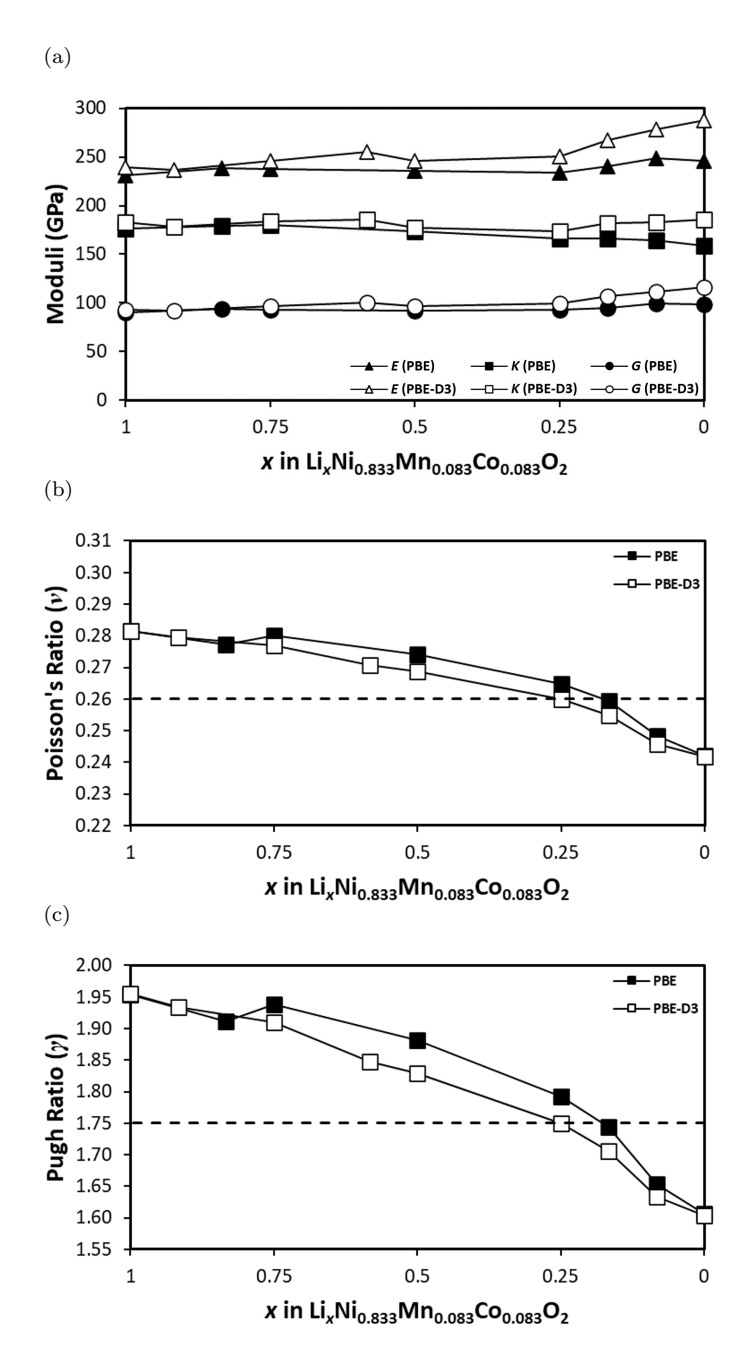


Figure 4: (a) Elastic moduli, (b) Poisson's Ratio, and (c) Pugh ratio of  ${\rm Li}_x{\rm NMC-811}$  as a function of Li concentration.

tions with and without dispersion. G shows an increase in magnitude for both functionals, however the inclusion of dispersion shows a greater increase as concentration decreases. For K, PBE shows a decrease until empty (x=0); however, dispersion effects cause a slight increase in K from x=0.25 to x=0. Because E is calculated from

both K and G, the divergence in the functionals is more exaggerated. Here, we see an increase with and without dispersion, but dispersion shows a more significant increase as we continue removing Li.

## 3.3.2. Ductility metrics

Both Poisson's ratio ( $\nu$ ) and the Pugh ratio ( $\gamma$ ) (shown in Fig. 4b and 4c, respectively) show identical trends as a function of Li concentration in Li<sub>x</sub>NMC-811. The fully lithiated cathode is predicted as (noticeably) ductile with both PBE and PBE-D3. From there, we show a continuous decrease in ductility throughout all Li concentrations when using PBE-D3, transitioning from ductile to brittle near x=0.25. For PBE, however, there is a slight increase in  $\nu$  and  $\gamma$  at x=0.75, with continual decreasing values thereafter. Here, the transition between ductile and brittle occurs around x=0.167.

For concentrations of Li between 0.167 and 0.75, if we compare the two functionals, both metrics of ductility appear to diverge before converging at both ends (x=0 and x=1). The most significant difference for the two functionals occurs at x=0.5 for both  $\nu$  and  $\gamma$ . For this specific point, we believe this difference comes from the (largest) decrease in the a,b-lattice vector when we include dispersion (0.12 Å). Furthermore, in the region where x<0.25 the metrics for ductility shift downwards such that the location at which the functionals cross the ductile/brittle boundary is different. However, the fully delithiated structure again shows no difference in the ductility metrics between the two functionals.

For further analysis of the electronic properties, we have included the PDOS results calculated with PBE and PBE-D3 in Fig. S2 and S3, respectively, where we see the general trend of depopulation of O(p) states through delithiation across the ductile/brittle boundary. For additional insight into structural changes, we have provided the radial distribution function for various atomic combinations calculated with PBE and PBE-D3 in Fig. S4 and S5, respectively, where one can see minimal structural changes occur through delithiation across the ductile/brittle boundary [41].

#### 4. Discussion

The overall consistent volume in  $\text{Li}_x\text{NMC-811}$  when calculated with PBE throughout the charging process would indicate that we would not expect a significant decrease in capacity due to strain through cycling. However, capacity loss is a known issue [54] and as such requires the need for further examination. The experimentally measured collapse of the c-lattice vector required us to further investigate the material properties using PBE-D3 (i.e., including dispersion). Overall, PBE-D3 provides better agreement with experimental findings for the structural and electrochemical properties of  $\text{Li}_x\text{NMC-811}$ . Even so, the calculation of the mechanical properties of  $\text{Li}_x\text{NMC-811}$  using both functionals has provided insight into the correlation between large changes in voltage and the ductile/brittle transition in this particular cathode.

The overall mechanical properties of this system are

changing such that once delithiation occurs to a level below x=0.25, a drastic transition in functionality occurs. For PBE-D3, the point at which the cathode crosses the ductile/brittle boundary not only corresponds to the largest change in the voltage profile, but it also coincides with the beginning of the experimentally proven lattice collapse. Thus, as the cathode passes this ductile/brittle boundary throughout the cycling process, the NMC-811 material is increasingly less capable of withstanding the additional stress that is associated with the deintercalation of Li ions; potentially explaining the corresponding lattice collapse, leading to a decreased ability to accommodate those ions (capacity), as well as cracking over time.

It has been shown experimentally that layered oxides commonly experience capacity loss after their first cycle, and it has been determined that if a cathode of this nature were to reach a completely delithiated state, that the maximum theoretical capacity cannot be retained [54]. Throughout the process of charge cycling,  $\text{Li}_x\text{NMC-811}$  will regularly cross the ductile/brittle boundary based on the degree to which it is charged. We believe that over time the repeated transition across the ductile/brittle boundary (as well as other changing mechanical properties) will be a key component in the overall lifetime performance of  $\text{Li}_x\text{NMC-811}$  as a battery cathode.

# 5. Summary and conclusions

By investigating the ductility of  $\text{Li}_x\text{NMC-811}$ , we have shown that the mechanical and electrochemical properties

are interwoven such that changes in either property corresponds to a significant change in the other. In particular, we have shown that the transition from ductile to brittle (as determined by both Poisson's ratio and the Pugh ratio) corresponds to the most significant change in voltage for Li<sub>x</sub>NMC-811 when using both PBE and PBE-D3 without significant corresponding changes in the electronic and/or physical structures. For the supercell that we have studied in this work, it is also below this concentration (x = 0.25)that the layered material will begin to completely empty layers of Li. Since the material is now brittle, it is our conjecture that during further delithiation that the battery will not be able to withstand this stress and the cathode will experience a significant decrease in capacity, while also facing a significant possibility of cracking due to significant collapse of its lattice. While most fractures of the cathode occur along grain boundaries or other material interfaces [65], the overall embrittlement of the bulk will contribute to the degradation of the entire material due to an inability to accommodate the repeated stress of charge cycling. It is our hope that this work inspires future investigations to further the understanding of the connection between a cathodes ductility and its structural and electrochemical performance. This phenomenon may open the door towards state-of-the-art materials whose mechanical properties can be reversibly controlled by electrochemical means.

## Acknowledgements

This work was supported by the Integrated Electronics Engineering Center (IEEC) at Binghamton University, and the National Science Foundation under Grant No. CBET-2028722. This work was performed using *Expanse*, a part of the Extreme Science and Engineering Discovery Environment (XSEDE), which is supported by NSF Grant No. 1928224 under allocation TG-DMR180009. We thank Dr. Hao Liu in the Department of Chemistry at Binghamton University and Dr. Louis Piper in the Electrochemical Materials Department at the University of Warwick for insightful discussions regarding this work.

# References

- M. S. Whittingham, Electrical Energy Storage and Intercalation Chemistry, Science 192 (4244) (1976) 1126–1127.
- [2] K. Mizushima, P. Jones, P. Wiseman, J. Goodenough, LixCoO2 (0<x<1): A new cathode material for batteries of high energy density, Materials Research Bulletin 15 (6) (1980) 783–789. doi:https://doi.org/10.1016/0025-5408(80)90012-4.</p>
- [3] M. S. Whittingham, Materials challenges facing electrical energy storage, MRS Bull. 33 (4) (2008) 411–419. doi:10.1557/mrs2008.82.
- [4] J. Speirs, M. Contestabile, The future of lithium availability for electric vehicle batteries, Renewable and Sustainable Energy Reviews 35 (2014) 183–193. doi:10.1016/j.rser/2014.04.018.
- [5] P. W. Gruber, P. A. Medina, G. A. Keoleian, S. E. Kesler, M. P. Everson, T. J. Wallington, Global lithium availability: A constraint for electric vehicles?, J. Ind. Ecol. 15 (5) (2011) 760–775. doi:10.1111/j.1530-9290.2011.00359.x.
- [6] G. Assat, J. M. Tarascon, Fundamental understanding and practical challenges of anionic redox activity in Li-ion batteries, Nat. Energy 3 (5) (2018) 373–386. doi:10.1038/s41560-018-0097-0.
- [7] R. Van Noorden, The rechargeable revolution: A better battery, Nature 507 (7490) (2014) 26–28. doi:10.1038/507026a.
- [8] Y. Koyama, I. Tanaka, H. Adachi, Y. Makimura, T. Ohzuku, Crystal and electronic structures of superstructural  $\mathrm{Li}_{1-\mathrm{x}}[\mathrm{Co}_{1/3}\mathrm{Ni}_{1/3}\mathrm{Mn}_{1/3}]\mathrm{O}_2$  ( $0\leq\mathrm{x}\leq1$ )], Journal of Power Sources 119-121 (2003) 644–648, selected papers presented at the 11th International Meeting on Lithium Batteries. doi:https://doi.org/10.1016/S0378-7753(03)00194-0.
- [9] H. Sun, K. Zhao, Electronic Structure and Comparative Properties of LiNi<sub>x</sub>Mn<sub>y</sub>Co<sub>z</sub>O<sub>2</sub> Cathode Materials , J. Phys. Chem. C 121 (11) (2017) 6002–6010. doi:10.1021/acs.jpcc.7b00810.
- [10] C. Xu, Z. Ahmad, A. Aryanfar, V. Viswanathan, J. R. Greer, Enhanced strength and temperature dependence of mechanical properties of Li at small scales and its implications for Li metal anodes, Proc. Natl. Acad. Sci. U. S. A. 114 (1) (2017) 57–61. doi:10.1073/pnas.1615733114.
- [11] M. S. Whittingham, Lithium Batteries and Cathode Materials, Chem. Rev. 104 (2004) 4271–4301. doi:10.1021/cr020731c.

- [12] R. Shepard, M. Smeu, Ab initio investigation of  $\alpha$  and  $\zeta$ -V2O5 for beyond lithium ion battery cathodes, J. Power Sources 472 (2020) 228096. doi:10.1016/j.jpowsour.2020.228096.
- [13] Y. Miao, P. Hynan, A. Von Jouanne, A. Yokochi, Current li-ion battery technologies in electric vehicles and opportunities for advancements, Energies 12 (6) (2019) 1074. doi:10.3390/en12061074.
- [14] R. Xu, H. Sun, L. S. de Vasconcelos, K. Zhao, Mechanical and Structural Degradation of  $\mathrm{LiNi}_x\mathrm{Mn}_y\mathrm{Co}_z\mathrm{O}_2$  Cathode in Li-Ion Batteries: An Experimental Study , J. Electrochem. Soc. 164 (13) (2017) A3333–A3341. doi:10.1149/2.1751713jes.
- [15] R. Xu, L. S. de Vasconcelos, J. Shi, J. Li, K. Zhao, Disintegration of Meatball Electrodes for LiNixMnyCozO2 Cathode Materials, Exp. Mech. 58 (4) (2018) 549–559. doi:10.1007/s11340-017-0292-0.
- [16] D. Kim, H. C. Shim, T. G. Yun, S. Hyun, S. M. Han, High throughput combinatorial analysis of mechanical and electrochemical properties of LiNixCoyMnzO2 cathode, Extreme Mechanics Letters 9 (2016) 439–448. doi:https://doi.org/10.1016/j.eml.2016.03.019.
- [17] E. J. Cheng, K. Hong, N. J. Taylor, H. Choe, J. Wolfenstine, J. Sakamoto, Mechanical and physical properties of LiNi0.33Mn0.33Co0.33O2 (NMC), J. Eur. Ceram. Soc. 37 (9) (2017) 3213–3217. doi:10.1016/j.jeurceramsoc.2017.03.048.
- [18] N. Y. Kim, T. Yim, J. H. Song, J. S. Yu, Z. Lee, Microstructural study on degradation mechanism of layered LiNi0.6Co0.2Mn0.2O2 cathode materials by analytical transmission electron microscopy, J. Power Sources 307 (2016) 641– 648. doi:10.1016/j.jpowsour.2016.01.023.
- [19] M. Lang, M. S. D. Darma, K. Kleiner, L. Riekehr, L. Mereacre,
   M. Ávila Pérez, V. Liebau, H. Ehrenberg, Post mortem analysis of fatigue mechanisms in LiNi0.8Co0.15Al0.05O2
   LiNi0.5Co0.2Mn0.3O2
   LiMn2O4/graphite lithium ion batteries, J. Power Sources 326 (2016) 397–409. doi:10.1016/j.jpowsour.2016.07.010.
- [20] G. Sun, T. Sui, B. Song, H. Zheng, L. Lu, A. M. Korsunsky, On the fragmentation of active material secondary particles in lithium ion battery cathodes induced by charge cycling, Extreme Mechanics Letters 9 (2016) 449–458. doi:https://doi.org/10.1016/j.eml.2016.03.018.
- [21] G. Li, Z. Zhang, Z. Huang, C. Yang, Z. Zuo, H. Zhou, Understanding the accumulated cycle capacity fade caused by the secondary particle fracture of LiNi1-x-yCoxMnyO2 cathode for lithium ion batteries, J. Solid State Electrochem. 21 (3) (2017) 673–682. doi:10.1007/s10008-016-3399-9.
- [22] P. Verma, P. Maire, P. Novák, A review of the features and analyses of the solid electrolyte interphase in Liion batteries, Electrochim. Acta 55 (22) (2010) 6332–6341. doi:10.1016/j.electacta.2010.05.072.
- [23] N. Liu, Z. Lu, J. Zhao, M. T. Mcdowell, H. W. Lee, W. Zhao, Y. Cui, A pomegranate-inspired nanoscale design for large-volume-change lithium battery anodes, Nat. Nanotechnol. 9 (3) (2014) 187–192. doi:10.1038/nnano.2014.6.
- [24] S. Watanabe, M. Kinoshita, T. Hosokawa, K. Morigaki, K. Nakura, Capacity fade of LiAlyNi1-x-yCoxO 2 cathode for lithium-ion batteries during accelerated calendar and cycle life tests (surface analysis of LiAlyNi1-x-yCo xO2 cathode after cycle tests in restricted depth of discharge ranges), J. Power Sources 258 (2014) 210–217. doi:10.1016/j.jpowsour.2014.02.018.
- [25] D. J. Miller, C. Proff, J. G. Wen, D. P. Abraham, J. Bareño, Observation of microstructural evolution in li battery cathode oxide particles by in situ electron microscopy, Adv. Energy Mater. 3 (8) (2013) 1098–1103. doi:10.1002/aenm.201300015.
- [26] L. Porz, T. Swamy, B. W. Sheldon, D. Rettenwander, T. Frömling, H. L. Thaman, S. Berendts, R. Uecker, W. C. Carter, Y. M. Chiang, Mechanism of Lithium Metal Penetration through Inorganic Solid Electrolytes, Adv. Energy Mater. 7 (20) (2017) 1701003. doi:10.1002/aenm.201701003.
- [27] S. Yu, D. J. Siegel, Grain Boundary Softening: A Potential Mechanism for Lithium Metal Penetration through Stiff Solid

- Electrolytes, ACS Appl. Mater. Interfaces 10 (44) (2018) 38151–38158. doi:10.1021/acsami.8b17223.
- [28] K. S. Nagy, D. J. Siegel, Anisotropic Elastic Properties of Battery Anodes, J. Electrochem. Soc. 167 (11) (2020) 110550. doi:10.1149/1945-7111/aba54c.
- [29] M. Woodcox, M. Smeu, Ab initio investigation of the elastic properties of CaxSn1-x alloys for use as battery anodes, J. Electrochem. Energy Convers. Storage 18 (November) (2021) 040903. doi:10.1115/1.4051210.
- [30] R. Xu, L. Scalco De Vasconcelos, K. Zhao, Computational analysis of chemomechanical behaviors of composite electrodes in Li-ion batteries, J. Mater. Res. 31 (18) (2016) 2715–2727. doi:10.1557/jmr.2016.302.
- [31] P. Hohenberg, W. Kohn, Inhomogeneous Electron Gas, Phys. Rev. B 136 (3B) (1964) 864–871.
- [32] W. Kohn, L. J. Sham, Self-consistent equations including exchange and correlation effects, Phys. Rev. 140 (4A) (1965) A1133–A1138.
- [33] W. Kohn, L. J. Sham, Quantum density oscillations in an inhomogeneous electron gas, Phys. Rev. 137 (6A) (1965) A1697. doi:10.1103/PhysRev.137.A1697.
- [34] G. Kresse, J. Hafner, Ab initio molecular dynamcis for liquid metals, Phys. Rev. B 47 (1) (1993) 558.
- [35] J. Furthmüller, G. Kresse, Efficiency of ab-initio total energy calculations for metals and semiconductors using a plane-wave basis set, Comput. Mater. Sci. 6 (1) (1996) 15–50.
- [36] G. Kresse, J. Furthmüller, Efficient iterative schemes for ab initio total-energy calculations using a plane-wave basis set, Phys. Rev. B 54 (16) (1996) 11169–11186.
- [37] P. E. Blöchl, Projector augmented-wave method, Phys. Rev. B 50 (24) (1994) 17953–17979.
- [38] J. D. Pack, H. J. Monkhorst, "special points for Brillouin-zone integrations"-a reply, Phys. Rev. B 16 (4) (1977) 1748–1749.
- [39] J. P. Perdew, K. Burke, M. Ernzerhof, Generalized gradient approximation made simple, Phys. Rev. Lett. 77 (18) (1996) 3865–3868.
- [40] S. Grimme, J. Antony, S. Ehrlich, H. Krieg, A consistent and accurate ab initio parametrization of density functional dispersion correction (DFT-D) for the 94 elements H-Pu, J. Chem. Phys. 132 (15) (2010) 154104. doi:10.1063/1.3382344.
- [41] See Supplemental Material at [URL will be inserted by publisher] for Table S1 which provides crystallographic information for the structure used in this work. Figure S1 shows the convex hull calculated for PBE and PBE-D3. Figures S2 and S3 show the PDOS for PBE and PBE-D3, respectively. Figures S4 and S5 show the radial distribution function for multiple atomic combinations at different concentrations for PBE and PBE-D3, respectively. Table S2 S3 which provide the relaxed lattice parameters, formation energy, and voltages for each concentration of Li using PBE and PBE-D3, respectively. And Table S4 which contains the numerical values of the mechanical properties for PBE and PBE-D3.
- [42] J.-M. Lim, T. Hwang, D. Kim, M.-S. Park, K. Cho, M. Cho, Intrinsic Origins of Crack Generation in Ni-rich LiNi<sub>0.8</sub>Co<sub>0.1</sub>Mn<sub>0.1</sub>O<sub>2</sub> Layered Oxide Cathode Material, Sci. Rep. 7 (2017) 39669. doi:10.1038/srep39669.
- [43] M. K. Aydinol, G. Ceder, First Principles Prediction of Insertion Potentials in LiMn Oxides for Secondary Li Batteries, J. Electrochem. Soc. 144 (11) (1997) 3832–3835. doi:10.1149/1.1838099.
- [44] M. K. Aydinol, A. F. Kohan, G. Ceder, Ab initio calculation of the intercalation voltage of lithium-transition-metal oxide electrodes for rechargeable batteries, J. Power Sources 68 (2) (1997) 664–668. doi:10.1016/S0378-7753(96)02638-9.
- [45] M. Aydinol, A. Kohan, G. Ceder, K. Cho, J. Joannopoulos, Ab initio study of lithium intercalation in metal oxides and metal dichalcogenides, Phys. Rev. B 56 (3) (1997) 1354–1365. doi:10.1103/PhysRevB.56.1354.
- [46] E. Deiss, A. Wokaun, J.-L. Barras, C. Daul, P. Dufek, Average Voltage, Energy Density, and Specific Energy of Lithium-Ion Batteries, J. Electrochem. Soc. 144 (11) (1997) 3877–3881.

- doi:10.1149/1.1838105.
- [47] S. K. Mishra, G. Ceder, Structural stability of lithium manganese oxides, Phys. Rev. B 59 (9) (1999) 6120–6130. doi:10.1103/PhysRevB.59.6120.
- [48] G. Ceder, A. Van Der Ven, Phase diagrams of lithium transition metal oxides: investigations from first principles, Electrochim. Acta 45 (1) (1999) 131–150. doi:10.1016/S0013-4686(99)00199-1.
- [49] J. Li, L. E. Downie, L. Ma, W. Qiu, J. R. Dahn, Study of the Failure Mechanisms of LiNi<sub>0.8</sub>Mn<sub>0.1</sub>Co<sub>0.1</sub>O<sub>2</sub> Cathode Material for Lithium Ion Batteries, J. Electrochem. Soc. 162 (7) (2015) A1401–A1408. doi:10.1149/2.1011507jes.
- [50] J. Zhu, G. Chen, Single-crystal based studies for correlating the properties and high-voltage performance of  $\text{Li}[\text{Ni}_x\text{Mn}_y\text{Co}_{1-x-y}]\text{O}_2$  cathodes, J. Mater. Chem. A 7 (2019) 5463–5474. doi:10.1039/c8ta10329a.
- [51] K. Märker, P. J. Reeves, C. Xu, K. K. Griffith, C. P. Grey, Evolution of Structure and Lithium Dynamics in  $\text{LiNi}_{0.8}\text{Mn}_{0.1}\text{Co}_{0.1}\text{O}_2$  (NMC811) Cathodes during Electrochemical Cycling, Chem. Mater. 31 (2019) 2545–2554. doi:10.1021/acs.chemmater.9b00140.
- [52] F. Xin, H. Zhou, X. Chen, M. Zuba, N. Chernova, G. Zhou, M. S. Whittingham, Li-Nb-O Coating/Substitution Enhances the Electrochemical Performance of the LiNi<sub>0.8</sub>Mn<sub>0.1</sub>Co<sub>0.1</sub>O<sub>2</sub> (NMC811) Cathode, ACS Appl. Mater. Interfaces 11 (2019) 34889-34894. doi:10.1021/acsami.9b09696.
- [53] K.-S. Lee, S.-T. Myung, K. Amine, H. Yashiro, Y.-K. Sun, Structural and Electrochemical Properties of Layered  $\mathrm{Li}[\mathrm{Ni}_{1-2x}\mathrm{Co}_x\mathrm{Mn}_x]\mathrm{O}_2$  (x=0.1-0.3) Positive Electrode Materials for Li-ion Batteries, J. Electrochem. Soc. 154 (10) (2007) A971–A977. doi:10.1149/1.2769831.
- [54] H. Zhou, F. Xin, B. Pei, M. S. Whittingham, What Limits the Capacity of Layered Oxide Cathodes in Lithium Batteries?, ACS Energy Lett. 4 (8) (2019) 1902–1906. doi:10.1021/acsenergylett.9b01236.
- [55] X. Dong, J. Yao, W. Zhu, X. Huang, X. Kuai, J. Tang, X. Li, S. Dai, L. Shen, R. Yang, L. Gao, J. Zhao, Enhanced highvoltage cycling stability of Ni-rich cathode materials via the self-assembly of Mn-rich shells, J. Mater. Chem. A 7 (2019) 20262–20273. doi:10.1039/c9ta07147d.
- [56] X. Fan, L. Chen, O. Borodin, X. Ji, J. Chen, S. Hou, T. Deng, J. Zheng, C. Yang, S.-C. Liou, K. Amine, K. Xu, C. Wang, Non-flammable electrolyte enables Li-metal batteries with aggressive cathode chemistries, Nature Nanotech. 13 (2018) 715— 722. doi:10.1038/s41565-018-0183-2.
- [57] J. Hu, Q. Wang, B. Wu, S. Tan, Z. Shadike, Y. Bi, M. S. Whittingham, J. Xiao, X.-Q. Yang, E. Hu, Fundamental Linkage Between Structure, Electrochemical Properties, and Chemical Compositions of LiNi<sub>1-x-y</sub>Mn<sub>x</sub>Co<sub>y</sub>O<sub>2</sub>, ACS Appl. Mater. Interfaces 13 (2021) 2622–2629. doi:10.1021/acsami.0c18942.
- [58] T. Ohzuku, A. Ueda, M. Nagayama, Electrochemistry and Structural Chemistry of LiNiO<sub>2</sub> (R3m) for 4 Volt Secondary Lithium Cells, J. Electrochem. Soc. 140 (7) (1993) 1862–1870. doi:10.1149/1.2220730.
- [59] M. Woodcox, J. Young, M. Smeu, Ab initio investigation of the elastic properties of bismuth-based alloys, Phys. Rev. B 100 (10) (2019) 104105. doi:10.1103/PhysRevB.100.104105.
- [60] M. Woodcox, J. Young, M. Smeu, Ab initio investigation of the temperature-dependent elastic properties of Bi, Te and Cu , J. Phys. Condens. Matter 32 (48) (2020) 485902. doi:10.1088/1361-648x/ababdf.
- [61] R. Hill, The elastic behaviour of a crystalline aggregate, Proc. Phys. Soc. Sect. A 65 (5) (1952) 349–354.
- [62] S. Pugh, Relations between the elastic moduli and the plastic properties of polycrystalline pure metals, The London, Edinburgh, and Dublin Philos. Mag. J. Sci. 45 (367) (1954) 823–843.
- [63] K. Min, K. Kim, C. Jung, S.-W. Seo, Y. Y. Song, H. S. Lee, J. Shin, E. Cho, A comparative study of structural changes in lithium nickel cobalt manganese oxide as a function of Ni content during delithiation process, J. Power Sources 315 (2016) 111–119. doi:10.1016/j.jpowsour.2016.03.017.

- [64] S. Hong, K. Zhao, Electronic Structure and Comparative Properties of  ${\rm LiNi_xMn_yCo_zO_2}$  Cathode Materials, J. Phys. Chem. C 121 (2017) 6002–6010. doi:10.1021/acs.jpcc.7b00810.
- [65] P. Li, Y. Zhao, Y. Shen, S. H. Bo, Fracture behavior in battery materials, JPhys Energy 2 (2) (2020) 022002. doi:10.1088/2515-7655/ab83e1.